Investigation on the discharge and charge behaviors of Li-CO_2 batteries with carbon nanotube electrodes

Xu Xiao[a], Peng Tan[a], Xingbao Zhu[b*], Yawen Dai[c], Chun Cheng[c], Meng Ni[c,d*]*

[a.] Department of Thermal Science and Energy Engineering, University of Science and Technology of China (USTC), Hefei 230026, Anhui, China

[b.] School of Physics, Harbin Institute of Technology, Harbin 150080, Heilongjiang, China

[c.] Department of Building and Real Estate, The Hong Kong Polytechnic University, Hung Hom, Kowloon, Hong Kong, China

[d.] Environmental Energy Research Group, Research Institute for Sustainable Urban Development (RISUD), The Hong Kong Polytechnic University, Hung Hom, Kowloon, Hong Kong, China

Corresponding Authors

*E-mail: pengtan@ustc.edu.cn (Peng Tan)

*E-mail: zhuxingbao008@163.com (Xingbao Zhu)

*E-mail: meng.ni@polyu.edu.hk (Meng Ni)

KEYWORDS: carbon nanotubes, current density, product morphology, discharge-charge behaviors, intrinsic mechanism.

ABSTRACT: Li-CO_2 batteries are regarded as promising electrochemical devices to simultaneously capture CO_2 and deliver electric energy. Although efforts are made to exploring reaction routes and developing effective catalysts, the discharge and charge behaviors at different current densities and the intrinsic mechanisms are not reported. Herein, a Li-CO_2 battery with a carbon nanotube electrode is investigated. It is found that with an increase of the current density, the discharge voltage plateau gradually

decreases. After the initial charge polarization, the following charge process shows a two-stage charge voltage profile where the first stage is sensitive to the applied current density while the second one is not. In addition, the electrode discharged at a lower current density has a higher voltage plateau of the first stage. The characterization results demonstrate that the discharge product is a combination of Li_2CO_3 and carbon in which crystalline Li_2CO_3 nanoparticles with the size of ~5 nm are distributed. Upon charging, rich nanopores with the sizes of 5~10 nm are observed, which may come from the shrinkage of both crystalline and amorphous Li_2CO_3. Even at the end of charge, Li_2CO_3 and carbon remain on the electrode, resulting in the irreversible process. Thus, the first charge stage is proposed to be the decomposition of crystal and amorphous Li_2CO_3, while the second charge stage with a high voltage is attributed to the blockage of transport channels and the accumulation of side products. Furthermore, for the first charge stage, a low discharge current density leads to small sizes of crystalline Li_2CO_3 combining with amorphous carbon in the products, increasing the transport resistance and causing a high charge voltage. On the contrary, a high discharge current density results in large sizes of Li_2CO_3 crystals, improving the overall conductivity and leading to a low charge voltage.

Introduction

Facing the rapid shrinkage of fossil fuel resources and the continuous increasing emission of carbon dioxide (CO_2) over the world, it is more imperative than ever to explore sustainable energy systems for relieving energy shortage and addressing environmental contamination.[1–4] Li-ion batteries, limited by the energy density (~350

Wh kg^{-1}),[5] are difficult to meet the energy-demanding requirement.[6] Metal-air batteries, due to the higher theoretical energy densities, are regarded as a promising electrochemical energy storage technology, especially for long-distance electric vehicles.[7] As an emerging family of metal-air battery systems, Li-CO_2 batteries which are assisted with the redox chemistry between Li and CO_2, harvest six times more energy density (1876 Wh kg^{-1}) than those of Li-ion batteries.[8] Ever since the concept of taking CO_2 as the fuel gas proposed in a primary large-capacity Li-CO_2 battery,[9] considerable research interests have been raised for both capturing greenhouse gas (mainly CO_2) and generating power supply.[10–12] Additionally, Li-CO_2 batteries have access to Mars exploration in a high CO_2 atmosphere (~96%), which offers excellent practical prospects in military and research fields.[5,13,14]

In spite of their great merits, many pivotal issues have impeded the development and practical application of Li-CO_2 batteries[15–17] The inactive Li_2CO_3, an insulator and an insoluble product, gradually covers the active sites of the electrode and is accumulated to a certain thickness upon discharge operation.[18] The dense passivation layer not only isolates the reaction intermediates from contact with Li^+ ions and/or electrons but also results in the substantial difficulty in the oxidation of carbonate products during the charging process.[19] This eventually leads to a large polarization between CO_2 reduction reaction (CORR) and CO_2 evolution reaction (COER),[2013] low round-trip efficiency during cycling,[21] and poor reversibility on recharge.[22] Meanwhile, the charge potential (often >4.5 V versus Li/ Li^+) is such high that inevitably induces the decomposition of electrolytes and electrodes to decrease the

cycle life.[23] Great efforts have been made to dealing with these hinders and enhancing electrochemical performance, such as exploring the reaction pathways on electrodes,[24,25] stabilizing the electrolytes,[26] and designing electrode structures for enhancing transport.[20] Among them, the development of available catalysts is the research hotspot of Li-CO_2 batteries, which accelerate the sluggish reaction kinetics and reduce the high overpotentials.[27,28]

Among various electrode materials, carbon materials, such as carbon powder (e.g., Super P), carbon nanotubes (CNTs), and graphene, have been employed owing to their high electronic conductivity, low cost, large porosity, and light weight.[29] Li et al. early showed that the Ketjin Black (KB) electrode obtained a discharge capacity of 1032 mAh g^{-1} at 30 mA g^{-1} and operated to 7 cycles at room temperature.[30] Zhou et al. introduced graphene and CNTs to improve the capacity to 14774 mAh g^{-1} and 8379 mAh g^{-1}, and the cycling stability to 20 times and 29 times at 50 mA g^{-1}, respectively.[29,31] Dai et al. fabricated B, N-codoped holey graphene to overcome rate capability and reversibility barriers, which exhibited an ultrahigh cyclability up to 200 times at a high current density of 1.0 A g^{-1}.[5] N-doped CNTs provided by Cheng et al. further enhanced the full capacity to 23328 mAh g^{-1}, prolonged a stabilized cycle life of over 360 cycles, and narrowed the potential gap to 1.96V at 1.0 A g^{-1}.[19] In addition to using carbon materials only, the decoration by metals or metal oxides has been widely explored, which can facilitate the interaction between Li_2CO_3 and carbon and markedly reduce the reaction barrier thermodynamically. For example, Mn_2O_3 decorated on KB drastically reduced the voltage gap to 1.4 V and kept running over 40

cycles (2000 h),[32] while the noble metal Ru dispersed on super P exhibited satisfactory polarization of 1.7 V and durable cycling stability of more than 70 times at 100 mA g^{-1}.[33] NiO/CNTs and Cu/N-doped graphene electrodes achieved a superior coulombic efficiency above 90% and cycling performance of over 40 cycles.[14,34] IrO_2/δ-MnO_2@carbon electrode could enable the operation of more than 300 cycles at 400mA g^{-1} and 200 cycles at 800mA g^{-1} without performance decay.[35] Mo_2C@CNT was utilized to stabilize intermediate product $Li_2C_2O_4$-Mo_2C and decreased the charge potential not exceeding 3.5 V.[36] In view of the complicated chemical/electrochemical reaction processes at the interface of CO_2-liquid electrolyte-solid electrode, in-depth research of fundamental reaction mechanism, especially the behavior feature during discharge and charge, can undoubtedly optimize the system components of Li-CO_2 batteries, and further provide useful guidelines for the design of the electrode materials.[8] Taking advantages of thermodynamic calculations and differential electrochemical mass spectrometry methods, the discharge mechanism is proposed as $4Li^+ + 4e^- + 3CO_2 \rightarrow 2Li_2CO_3 + C$.[33] Additionally, the porous gold electrode was introduced to track amorphous carbon apart from conspicuous Li_2CO_3, and the observation of Li_2CO_3 and carbon is in accordance with other research.[37,38] Subsequently, the insufficiency of the supply rate via the low Li^+ ion concentration of 50×10^{-3} M and the CO_2 volume ratio of 1:5 to Ar has strongly evidenced the formation of oxalate species at the beginning of discharge.[25] Besides the unique reaction process during discharge, two crucial charge mechanisms have been proposed, including the electrochemical self-decomposition of solid Li_2CO_3 using

carbon electrode and the reversible reaction of Li_2CO_3 and amorphous carbon species using effective catalysts.[19] Zhou et al. have demonstrated the evolution of gaseous CO_2 as the main product without any O_2 upon charging, while the track of surperoxide radicals (O_2^-) result in the decomposition of organic electrolyte.[39] Subsequently, the missing O_2 found by Freunberger et al. was detected through its corresponding chemical probes.[40] Moreover, the kinetic factor can alter the charge pathway in which the individual decomposition of Li_2CO_3 can proceed via either a three-electron process ($2Li_2CO_3 \rightarrow 4Li^+ + 2CO_2 + O_2^- + 3e^-$) or a four-electron process that involves the evolution of O_2 ($2Li_2CO_3 \rightarrow 4Li^+ + 2CO_2 + O_2 + 4e^-$).[25] Although the above-mentioned investigations provide the possible discharge and charge reaction mechanisms, it is noteworthy that owing to the solid products formed under discharge, the charge process is not a sole process that should be considered with the connection to the discharge process. In a similar situation of Li-O_2 batteries where the product is solid Li_2O_2,[41] the research demonstrates that the batteries discharge at different current densities can greatly affect the charge behaviors owing to the different product morphologies (e.g., toroid or film)[42] and structures (e.g., amorphous).[43] However, the electrochemical behaviors of Li-CO_2 batteries at different discharge and charge current densities and the intrinsic mechanisms have not been reported yet.

Herein, the discharge and charge behaviors of a Li-CO_2 battery under different current densities were investigated in this work. As CNTs have been widely applied with remarkable electrochemical performance in Li-CO_2 batteries, CNT-based

electrodes were used as a representative of carbon materials. We first tested the electrochemical performance of this electrode at different discharge and charge current densities with a fixed capacity. Then, the compositions and morphologies of the discharged and charged electrodes were characterized. Moreover, combined with the observation, the formation and decomposition processes of the hybrid products were proposed, and the origin of charge potential at different current densities was revealed. This works provides insights into the mechanisms of Li-CO_2 batteries, and will benefit the development of effective electrode materials and operating strategies for improved energy efficiency.

Experimental

Electrode fabrication

The CNT electrodes were fabricated as follows: a mixture of multi-walled CNTs with the diameter of 8-15 nm, length of 8-12 μm, and surface area of 233 m^2 g^{-1} and polytetrafluoroethylene (PTFE) as the binder with the mass ratio of 9: 1 was uniformly sprayed on the surface of a carbon paper (TGP-H-060, 210 μm thickness). After drying for 60 min, the electrode was annealed in the muffle furnace in the air at 250 ^oC and 340 ^oC for 1 h, respectively, to make the binder uniformly distribute and well connect with the CNTs. Later, electrodes were punched into circular pieces with a diameter of 10 mm, and the loading of CNTs was measured to be ~0.8mg cm^{-2}.

Battery assembly and tests

The electrochemical performance of the CNT electrode was measured by a home-made Li-CO_2 battery, which was assembled in an argon-filled glove box

(Etelux, Lab 2000) with the oxygen and water concentration of less than 1 ppm. The type of lithium metal electrode is 16 mm in diameter and 0.6 mm in thickness. The Whatman glass fiber was used as the separator. The punched CNT electrode is saturated with 1.0 M lithium bis(trifluoromethanesulfonyl)imide in tetraethylene glycol dimethyl ether (LiTFSI/TEGDME) electrolyte, which was saved in the glove box after drying over molecular sieves. The galvanostatic discharge and charge tests were performed to investigate the CO_2 reduction and evolution processes using a fixed capacity mode (Neware, CT-3008W). Two groups of experiments were conducted: the first one was discharged at different current densities of 50, 100, and 150 mA g^{-1}, and charged at the same current density of 50 mA g^{-1}; and the other one was discharged at the same current density of 150 mA g^{-1}, and charged at different current densities of 50, 100, and 150 mA g^{-1}. Both discharge and charge tests were carried out at room temperature under a fixed capacity of 1000 mAh g^{-1}.

Material characterization

The Li-CO_2 batteries after tests were disassembled and the CNT electrodes were rinsed with the dimethyl ether (DME) solvent in the argon-filled glove box. The washed electrodes were dried overnight in the vacuum chamber before the following characterization analyses. The signal of Li_2CO_3 product was confirmed by using Philips high-resolution X-ray diffraction system (XRD, model PW 1825) with a Cu-Kα radiation source of 40 keV and Fourier-transform infrared-attenuated total reflectance (FTIR-ATR) spectroscopy on an infrared spectrometer (Thermo Fischer Scientific) with a diamond crystal at the wavenumber range of 750-1750 cm^{-1}. The

track of C element was examined by a Jobin-Yvon Horiba LabRam HR Evolution Raman spectrometer with a 633 nm laser. The morphologies of the products were collected with field-emission scanning electron microscopy (FESEM, JEOL-7500 F) at an accelerating voltage of 2.0 kV. The discharged and charged electrodes were tracked with the high-resolution transmission electron microscopy (HRTEM, JEOL-2010F) at 200 kV, and the scanning transmission electron microscope (STEM) mapping was used to demonstrate the elemental distribution at 15 kV.

Results and discussion

As shown in **Figure 1a** the porous air electrodes made of CNTs were discharged to a fixed capacity of 1000 mAh g^{-1} under current densities of 50, 100, 150 mA g^{-1}, respectively. During discharge, the voltage plateau is about 2.72 V at a low current density of 50 mA g^{-1}, which continuously decreases to 2.65 V at 100 mA g^{-1}, and 2.59V at 150 mA g^{-1}. To characterize the discharge products, the electrodes were first examined by XRD, as shown in **Figure 1b.** Under the CO_2 atmosphere, in addition to the two diffraction peaks of the CNT substrate, the diffraction peaks at 21.34°, 30.64° and 31.79° can be indexed to the (110), ($\bar{2}02$), and (002) lattice planes of Li_2CO_3 (JCPDS #87-0729), and the other peaks indexed to Li_2CO_3 are marked as the shaded areas, indicating the formation of Li_2CO_3. The average crystal size of Li_2CO_3 is estimated by the results of XRD from 1.8 nm (at the current density of 50 mA g^{-1}) to 3.8 nm (at 100 mA g^{-1}) and then to 5.4 nm (at 150 mA g^{-1}). The existence of Li_2CO_3 was further confirmed by FTIR, which corresponds to the absorbance peaks at around 1415 and 860 cm^{-1} (marked as the shaded areas), as presented in **Figure 1c**.

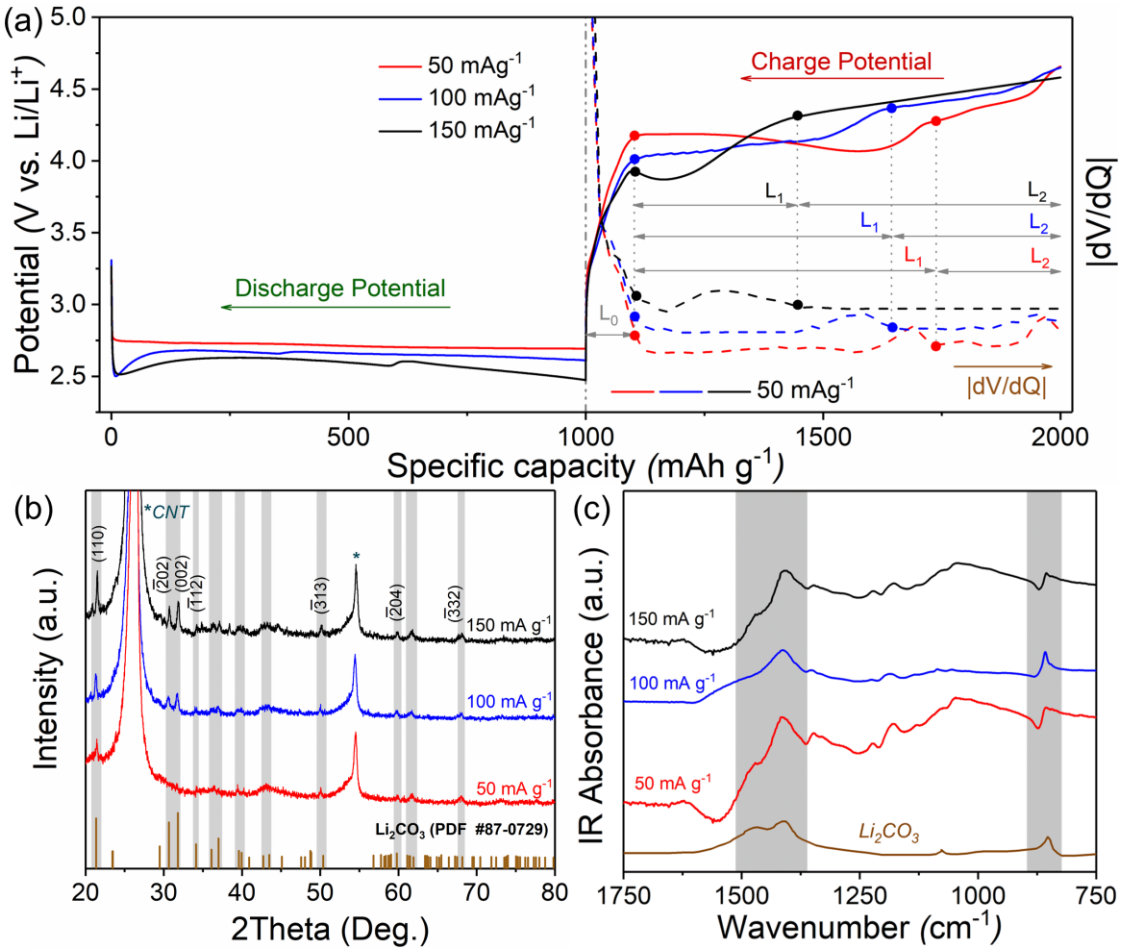

Figure 1. Electrochemical performance and characterization of the CNT-based electrodes: (a) discharge-charge voltage profiles with a cut-off capacity of 1000 mAh g^{-1} at different discharge current densities (50, 100, 150 mA g^{-1}) and a same charge current density of 50 mA g^{-1}. The |dV/dQ| (unit: V $(mAh\ g^{-1})^{-1}$) of the above charge voltage curves are also presented, and the scale is adjusted to clearly show the three curves. (b) XRD patterns and (c) FTIR spectra after discharge.

To provide insight into the discharge behaviors of the CNT electrode, we examined the morphologies of the pristine and discharged electrodes at different current densities, and the SEM images are shown in **Figures 2a-d**. For the pristine

electrode, CNTs are tangled with each other to form a porous network, and the surfaces of CNTs are clean (**Figure 2a**). While after discharge, the smooth surfaces turn into rough and are coated with solid products, as demonstrated in **Figures 2b-d**. Besides, with an increase of the discharge current, the product morphology converts from floccules or sheet aggregations (at 50 mA g^{-1}) to small particles (at 100 mA g^{-1}) and then to thin-platelets (at 150 mA g^{-1}). To further examine the structure of the products, TEM characterization of the electrode discharged at 150 mA g^{-1} was carried out, as illustrated in **Figure 3**. The products grown on CNTs are composed of numerous small particles (**Figure 3a** and **3c**), and some "dark dots" can be observed. The selected area electron diffraction (SAED) pattern in the inset corresponds to the (110), $(\bar{3}11)$, and $(\bar{4}23)$ lattice planes of Li_2CO_3, verifying that Li_2CO_3 is formed in the products. From the HRTEM in **Figure 3b**, several visible nanoparticles with the grain sizes of roughly 5 nm are distributed among the products, consistent with the calculation results from XRD. The zoomed-in perspective in the inset shows the well-resolved lattice fringes with an interplanar spacing of 0.211 nm, which corresponds to the (112) plane of Li_2CO_3. Thus, the "dark dots" in the products are crystalline Li_2CO_3, while "light parts" are speculated to be the amorphous Li_2CO_3 and carbon according to the electrochemical reaction occurred in Li-CO_2 batteries.[33] To confirm this, the element mappings in **Figure**s **3d-f** illustrate that besides CNTs, C and O elements are distributed in the product region (the center of **Figure 3c**). Apart from TEM observation of C element, the Raman spectra of the pristine, discharged, partially charged, and fully charged electrodes were tested to further confirm the C

evolution. As shown in **Figure 4**, it is revealed that two main characteristic peaks detected at 1340 and 1581 cm^{-1} correspond to the D and G bands of carbon species, respectively, and a broad peak at 1120 cm^{-1} that is corresponding to Li_2CO_3 emerges at discharge. The intensity ratio of D and G bands (I_D/I_G) converts from 1.44 (the pristine electrode) to 1.71 (the discharged electrode), demonstrating that the amorphous carbon (disordered phase) is formed as the discharge process proceeds. Hence, the combination of characterization succeeds in providing evidence of the track of C elements. Thus, the discharge products are demonstrated to be a combination of Li_2CO_3 and C, and crystalline Li_2CO_3 particles are distributed in the amorphous phases.

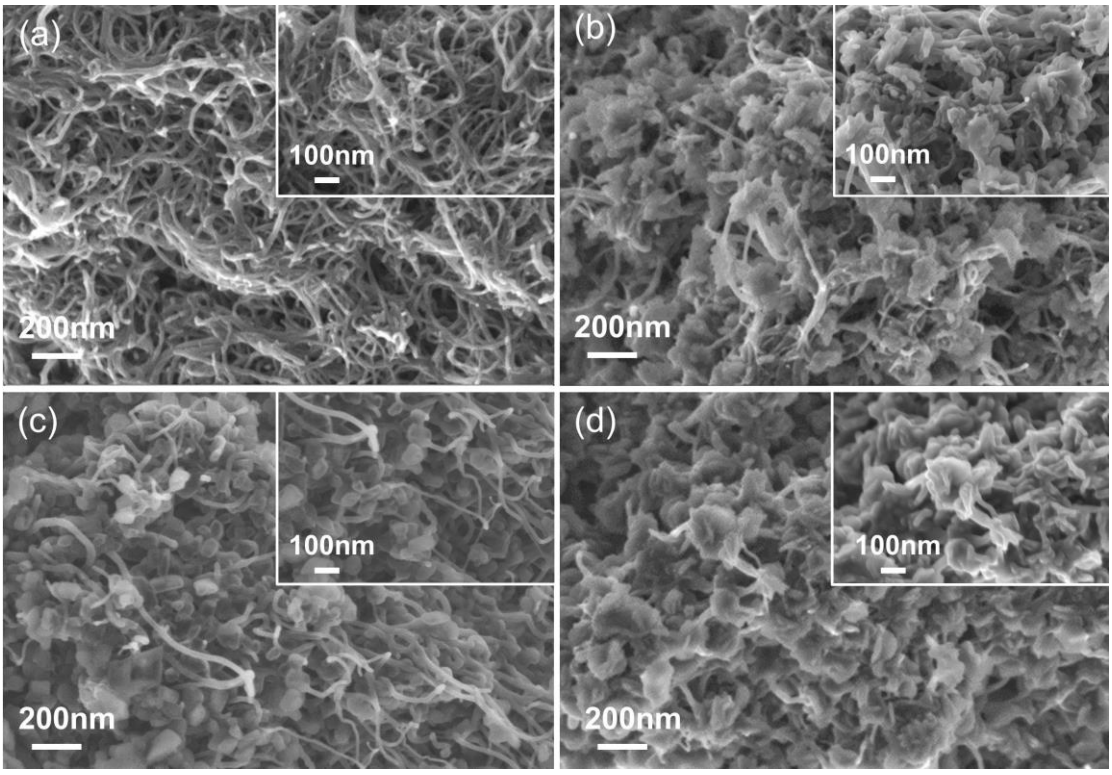

Figure 2. SEM images of (a) pristine and (b-d) discharged electrodes at various current densities: (b) 50, (c) 100, and (d) 150 mA g^{-1} with a cut-off capacity of 1000 mAh g^{-1}.

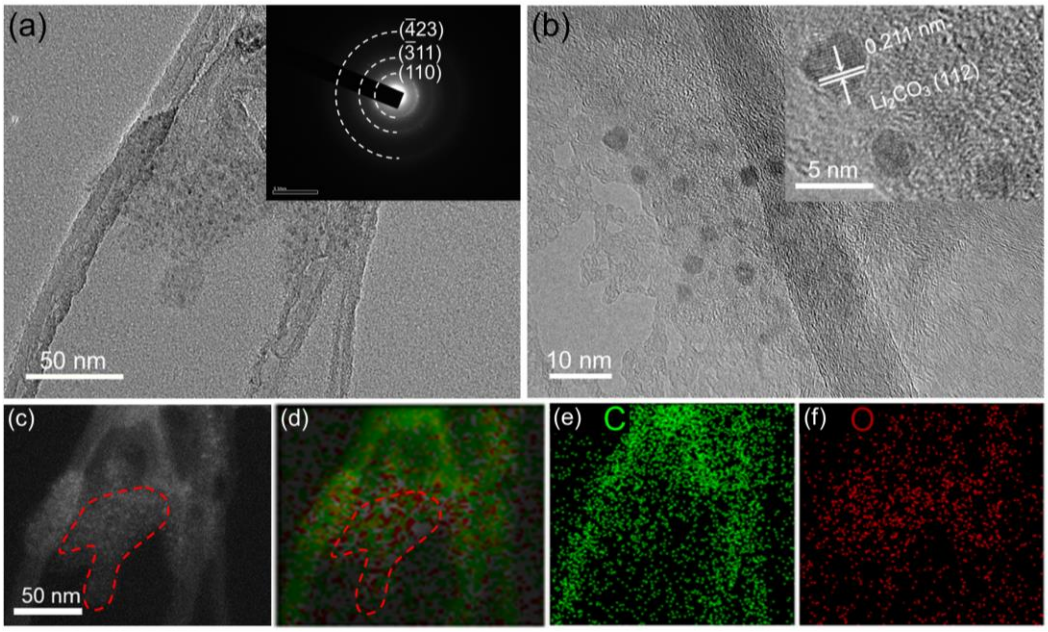

Figure 3. TEM images of the CNT electrode after discharge with a cut-off capacity of 1000 mAh g^{-1} at current density of 150 mA g^{-1}: (a) CNTs with the discharge products, and the inset shows the SAED pattern; (b) HRTEM images of the products, and the inset shows the solid particles with a high-magnification; (c) Simultaneously acquired image and (d) EDS spectrum imaging for chemical maps of C and O; (e-f) STEM element mapping of (e) C and (f) O.

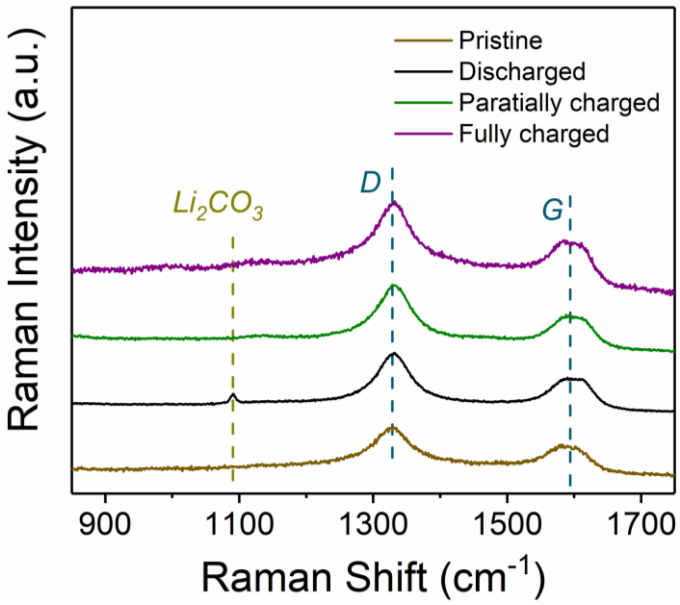

Figure 4. Ex-situ Raman spectra of CNT electrodes at the pristine stage, the discharged stage with a cut-off capacity of 1000 mAh g^{-1}, the partially charged stage with a cut-off capacity of 400 mAh g^{-1}, and the fully charged stage with a cut-off capacity of 1000 mAh g^{-1}, respectively.

The discharged electrodes at various current densities were then charged at the same current density of 50 mA g^{-1}. As shown in **Figure 1a**, after the initial charge polarization, the following voltage profiles exhibit two stages: in the first stage, a lower voltage plateau is presented, which even decreases with the charge process; while in the second stage, the voltage suddenly increases and keeps increasing till the end of charge. To investigate the reaction process at different charge states, the results of |dV/dQ| are used, which reflect the changes of conductivity upon charging. The outlines of |dV/dQ| can be roughly divided into three stages: the rapid increase stage owing to the charge polarization (L_0), the stage with the appearance of characteristic peaks (L_1), and the relatively flat stage (L_2). It is found that the electrode discharged at

a low current density (e.g., 50 mA g^{-1}) has a longer first charge-voltage stage (L_1). Additionally, with an increase of the discharge current density, the charge voltage plateau decreases in the first stage, but increases in the second stage. To elucidate the mechanism during the charge process, we conducted another experiment, in which the CNT electrodes were discharged at the same current density of 150 mA g^{-1} and then charged using different current densities of 50, 100, and 150 mA g^{-1}. As displayed in **Figure 5a**, the two-stage charge voltage profiles are observed, which is in accordance with the phenomena in **Figure 1a**. In addition, the results of |dV/dQ| indicate that the length of each stage almost keeps constant when the charge voltage changes. In the first charge stage (L_1), the charge voltage increases clearly with an increase of the charge current density; but in the second stage (L_2), the charge voltages almost exhibit the same value. In other words, the charge voltage is more sensitive to the current density in the first stage (at around 400 mAh g^{-1}) but becomes insensitive in the second stage. Thus, three crucial points during charge (A, B, and C) were employed to study the decomposition of discharged products. The point A is the initial charge stage (which is also the termination of the discharge process), while point B is the turning point between sensitive and insensitive stages during charge, and point C is the termination of the charge process. The XRD patterns of the electrodes at different stages are investigated in **Figure 5b**. At point A, the three strong peaks are assigned to be the (110), ($\bar{2}02$), and (002) planes of Li_2CO_3, which become weaker and even disappear at point B, indicating the decomposition of Li_2CO_3. The FTIR spectra in **Figure 5c** and the Raman spectra in **Figure 4** also show that Li_2CO_3 is reduced at

point B. Meanwhile, the I_D/I_G ratio of the Raman spectra converts from 1.71 (point A) and to 1.74 (point B) and then to 2.01 (point C), revealing that amorphous carbon still remains on the electrode upon charging.

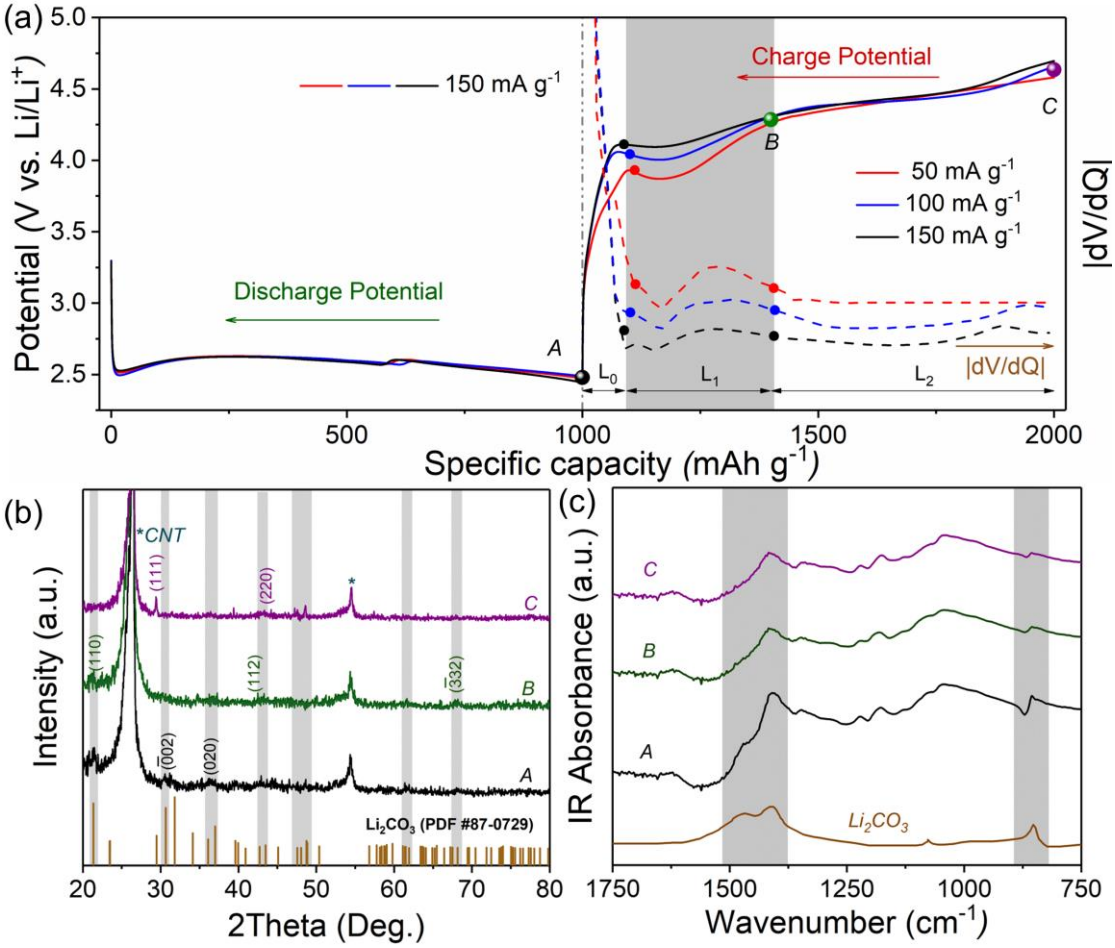

Figure 5. Electrochemical performance and characterization of the CNT-based electrodes at different stages: (a) discharge-charge profiles with a cut-off capacity of 1000 mAh g^{-1} at a same discharge current density of 150 mA g^{-1} and different charge current densities (50, 100, and 150 mA g^{-1}). The |dV/dQ| (unit: V (mAh g^{-1})$^{-1}$) of the above charge voltage curves are also presented with the stage L_1 marked as the shaded area, and the scale is adjusted to clearly show the three curves. (b) XRD patterns and (c) FTIR spectra at the different charged stages.

Further, the morphology of the electrode charged at 400 mAh g^{-1} at point B was characterized. Compared with the electrode at point A (**Figure 2d**), the surfaces of the thin-platelet-like products are melting and become irregular, as shown in **Figure 6a**. From the TEM image in **Figure 7a**, no "dark dots" can be observed. Surprisingly, rich pores are detected to embed inside the residual products, most of which are close to the surfaces of CNTs. From the high-resolution image in **Figure 7b**, no crystalline Li_2CO_3 nanoparticles are presented. Instead, the sizes of pores are 5~10 nm, which are equal to or greater than those of Li_2CO_3 nanoparticles (~5 nm) in **Figure 3b**. Previous investigations have shown that the crystalline Li_2CO_3 has a little higher diffusivity and ionic conductivity than the amorphous phase.[44–46] Thus, the amorphous Li_2CO_3 may provide charge transport channels for the delithiation and charge transfer process, inducing the preferential decomposition of crystal nanoparticles. These nanopores indicate that the crystalline Li_2CO_3 nanoparticles are consumed and the amorphous region also contributes to being excavated upon charge. Combining with the TEM results, the characteristic peaks of the |dV/dQ| arise from the phase transition of the crystal Li_2CO_3 in the first charge stage (L_1). Certainly, the average sizes of crystalline Li_2CO_3 and the states with C species can affect the intensity, width, and position of the peak, which are related to the discharge current density. Consequently, the battery discharged at different current densities has different charge voltage profiles even at the same charge current density. From **Figures 7c-f**, the element mappings of C and O illustrate the residual carbon and Li_2CO_3, consistent with the XRD, FTIR, and Raman results.

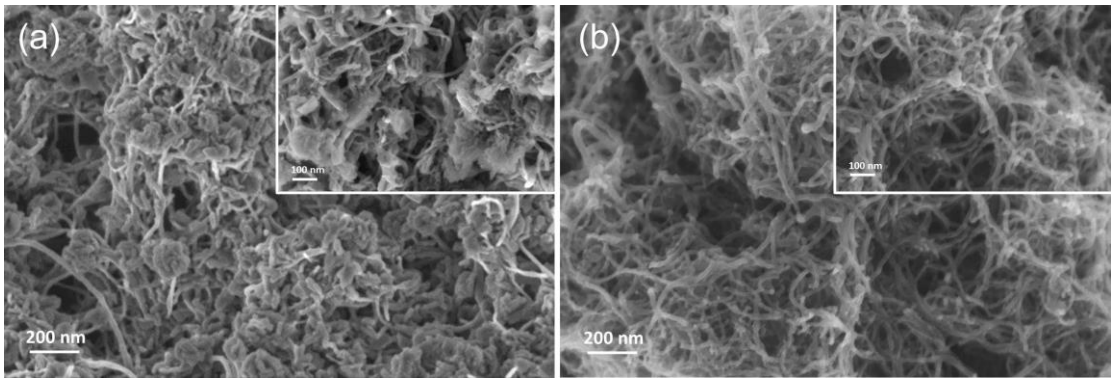

Figure 6. SEM images of the CNT electrode charged with the current density of 150 mA g^{-1} at (a) point B (the turning point between sensitive and insensitive stages) and (b) point C (the end of charge).

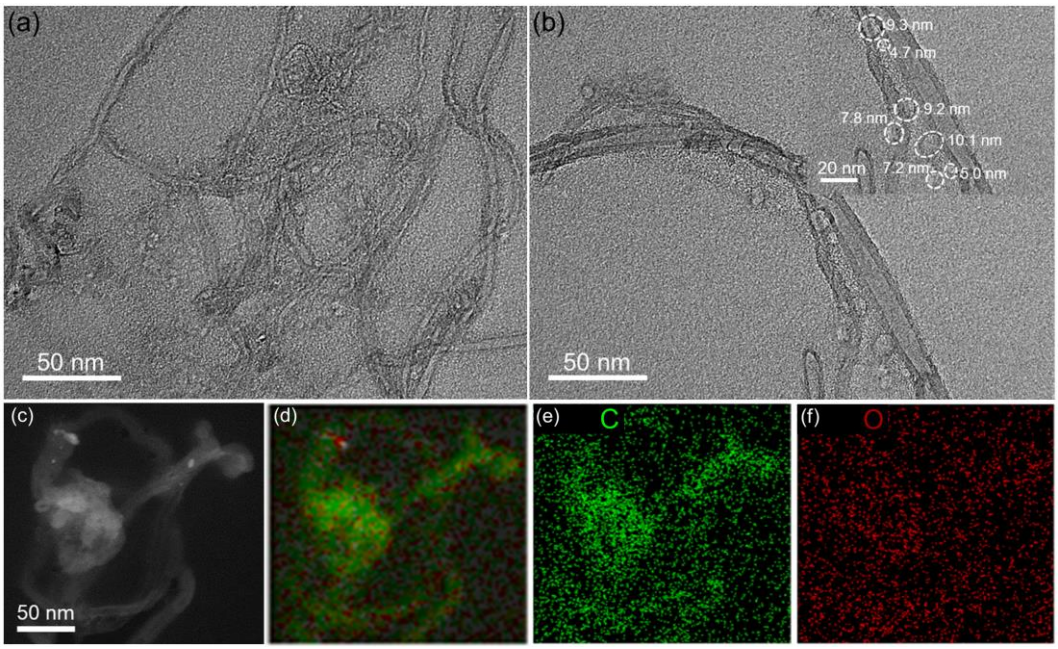

Figure 7. TEM images of the CNT electrode at point B: (a) CNTs with the discharge product; (b) HRTEM images of the residual products, and the inset shows the pore sizes (marked with white circles); (c) Simultaneously acquired image and (d) EDS spectrum imaging for chemical maps of C and O; (e-f) STEM element mapping of (e) C and (f) O.

At point C, from the XRD patterns in **Figure 5b**, most peaks assigned to Li_2CO_3

disappear, while some peaks still remain, indicating the remaining of Li_2CO_3 in the products. The result can be confirmed by the FTIR spectra in **Figure 5c**, although the surfaces of CNTs seem to be smooth without visible product particles in **Figure 6b**. As shown in **Figure 4**, Raman spectra also evidence that the high I_D/I_G ratio (2.01) means undecomposed carbon, while may induce the decomposition of the electrolyte and/or carbon electrode due to the high charge potential (e.g., > 4.3 V) at the second charge stage, with the results of |dV/dQ| presented in **Figures 1a and 5a**. The reason may be as follows: first, the electrochemical reactions occur on the carbon electrode is irreversible, during which only part of targeted Li_2CO_3 can be decomposed as reported by Zhou et al.;[25] second, carbon is inactive as the catalyst towards the decomposition of solid Li_2CO_3,[30] resulting in a high charge voltage (i.e., >4.5 V) that causes the decomposition of CNTs and the electrolytes.[47] As a result, Li_2CO_3 can be detected even after full charge, indicating that a Li-CO_2 battery can hardly be stably discharge-charge cycled using a CNT electrode only.

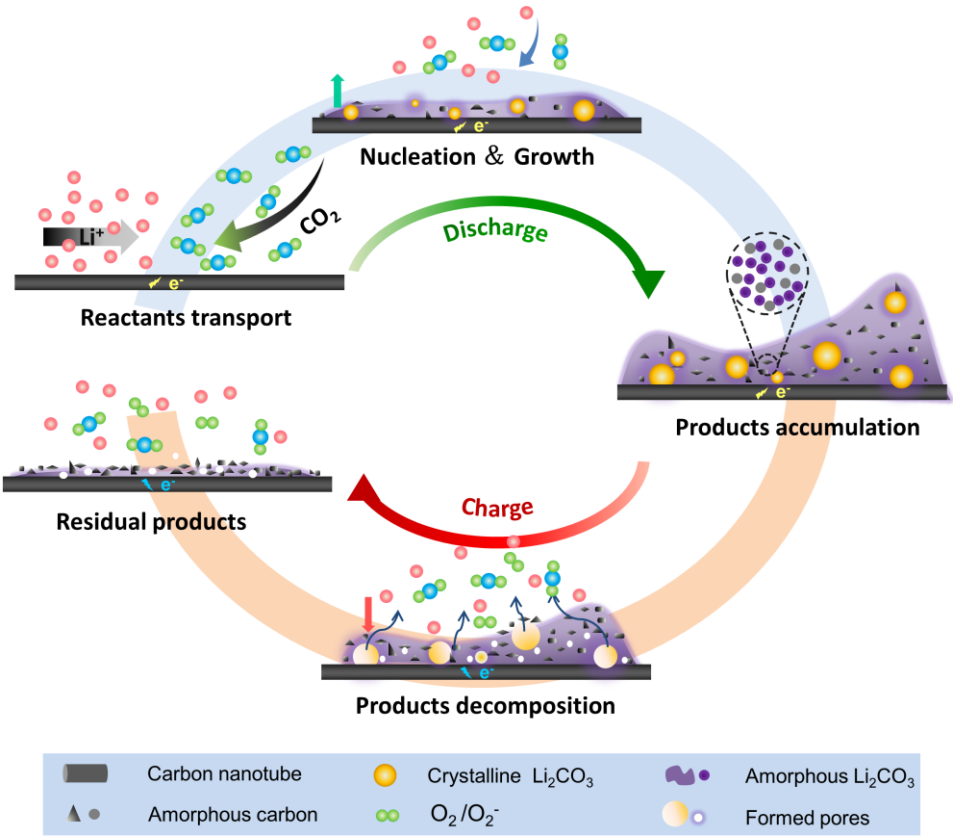

Figure 8. Schematic illustration of the proposed discharge and charge mechanisms of Li-CO_2 batteries with CNT electrodes.

Based on the above results, the discharge and charge mechanisms of Li-CO_2 batteries with CNT electrodes are proposed as schematically illustrated in **Figure 8**. Upon discharging, CO_2 dissolved in the electrolyte is reduced on the electrode surface, which meets Li^+ and forms carbon and Li_2CO_3. Since carbon is insoluble in the non-aqueous electrolyte, the generated carbon will immediately precipitate on the electrode surface. While for Li_2CO_3, it may dissolve in the electrolyte to a certain amount,[48] and then start to precipitate when the concentration reaches the saturation value. As a result, nucleation and growth of Li_2CO_3 can occur on the electrode, resulting in the formation of crystalline Li_2CO_3 nanoparticles. Besides, amorphous Li_2CO_3 can also form at the places without sufficient nucleation sites. Thus, at the end

of discharge, the products present the morphology composed of numerous nanoparticles in which crystalline Li_2CO_3 nanoparticles are well distributed (**Figure 3**). Upon charging, the decomposition of Li_2CO_3 crystal nanoparticles (~5nm) and amorphous phases causes the remaining carbon to get together with each other, building up a layer of the visible self-supporting shell and further leads to the formation of nanopores with the size of 5~10 nm after the first charge stage (**Figure 7**). With the charge deepening, as carbon can hardly be decomposed using the CNT electrode (**Figure 4**),[19] the shrinking Li_2CO_3 is surrounded by extremely passivated carbon film and turns into "isolated islands". In addition, the high charge voltage causes the decomposition of electrode and electrolyte, resulting in carbonate-based side products that passivate the electrode surfaces.[49,50] Thus, even after fully charged, the electrode is distinct from the pristine one, as confirmed by the results of Raman, XRD, and FTIR shown in **Figures 4**, **5b**, and **5c**.

According to the proposed mechanisms, the discharge and charge behaviors in our experiments are explained as follows: The reaction interfaces of Li_2CO_3/electrode and Li_2CO_3/electrolyte play dominant roles in the charge reactions of Li-CO_2 batteries. Different contact modes determine the mass transfer resistance and electrons transport. In virtue of the priority of electric flow, the superficial Li_2CO_3 toward the electrode surface is preferentially consumed, and the product collapses in a certain direction. In addition, thanks to the good electronic conductivity of carbon involved in the products, the decomposition of Li_2CO_3 can also initiate locally at the Li_2CO_3/electrolyte interface at the same time. In both cases, the product thickness is reduced along with

charging, decreasing the transport resistance of species and electrons, leading to a stable and even decreasing charge voltage in the first stage. Thus, the plateau value depends on the effective conductivity of the formed products and is sensitive to the applied charge current density. At a low discharge current density (e.g., 50 mA g^{-1}), the low electrochemical reaction rate leads to a low formation rate of Li_2CO_3. Consequently, Li_2CO_3 can grow to a small size with the amorphous carbon to form a well-distributed structure, which increases the transport resistance of species and electrons to resolve the crystalline particles, leading to a high charge voltage plateau (**Figure 1a**). On the contrary, the high discharge current density (e.g., 150 mA g^{-1}) drives products to nucleate and grow very rapidly, resulting in large sizes of Li_2CO_3 particles, improving the overall conductivity and leading to a low charge voltage plateau. The similar phenomena have also been reported in non-aqueous Li-O_2 batteries, in which the Li_2O_2 formed at lower current densities exhibits higher charge voltage.[51] After the first charge stage, Li_2CO_3 nanoparticles massively decompose, accompanied with the amorphous Li_2CO_3 around the crystals, which may break the architecture for transport channels (e.g., forming pores) of both ion deintercalation (e.g., Li^+) and the gas emission (e.g., CO_2), causing the sharp jump of the charge voltage. In the second charge stage, the residual amorphous Li_2CO_3 is tightly wrapped with carbon. Since the produced carbon is hard to decompose on the surfaces of CNTs, the passivated carbon may affect and/or even block the species transport channels (e.g., CO_2 and Li^+), giving to a very high charge voltage. As the charging process goes deeper, the applied current density may drive the decomposition of the electrolyte

instead of the discharge products when the voltage is higher than 4.3 V. Consequently, the second charge stage is insensitive to the charge current density. While for the products formed at a lower current density (e.g., 50 mA g^{-1}), due to the large number of crystal Li_2CO_3, the first charge stage is longer so that the charge voltage only climbs near the end of charge, leading to a shorter second charge stage. Thus, the growth mode of discharge products strongly influences the charge voltage. Tuning the crystalline structures and improving the activity of electrode materials toward the decomposition of discharge products for both carbon and Li_2CO_3 are worth in-depth studies.

Conclusions

In summary, we have investigated the discharge and charge behaviors of Li-CO_2 batteries with CNT electrodes under different current densities. When increasing the discharge current density, the discharge voltage plateau gradually decreases, and product morphology shifts from floccules or sheet aggregations to small particles and then to thin-platelets. The product compositions are detected to be a combination of Li_2CO_3 and carbon, in which crystalline Li_2CO_3 particles are distributed in the amorphous Li_2CO_3 and carbon phases. After the initial charge polarization, a two-stage charge voltage profile can be exhibited in the following charge process in which the first stage is sensitive to the applied current density while the second one is insensitive. In addition, for the electrode discharged at a low current density, the voltage plateau of the first stage is high. Through the optical observation, it is found after the first charge stage, the crystalline Li_2CO_3 nanoparticles disappear, but rich

nanopores with the size of 5~10 nm are embedded inside the residual products. Further characterization indicates that both the crystalline and amorphous Li_2CO_3 is shrinking upon charging, which may be the reason for the formation of nanopores. Even at the end of charge, Li_2CO_3 and carbon remain on the electrode, resulting in the irreversible process. Thus, we propose that the first stage is associated with the decomposition of crystal and amorphous Li_2CO_3, and the break of transport channels causes the sharp jump of the charge voltage, while the second stage is attributed to the blockage of transport channels and the accumulation of side products. Further, a low discharge current density can lead to the small sizes of crystalline Li_2CO_3 particles combining with amorphous carbon in the products, increasing the transport resistance of species and electrons and causing a high charge voltage plateau. On the contrary, the high discharge current density (e.g., 150 mA g^{-1}) drives products to nucleate and grow very rapidly, resulting in large sizes of Li_2CO_3 crystals, improving the overall conductivity and leading to a low charge voltage plateau The findings in this work provide will benefit the development of effective electrode materials and operating strategies for improving the energy efficiency of Li-CO_2 batteries.

AUTHOR INFORMATION

ORCID

Peng Tan: 0000-0001-5750-0477

Meng Ni: 0000-0001-5310-4039

Notes

The authors declare no competing financial interest.

ACKNOWLEDGMENT

P. Tan thanks the funding support from CAS Pioneer Hundred Talents Program (KJ2090130001), USTC Research Funds of the Double First-Class Initiative (YD2090002006), and USTC Tang Scholar. X.B. Zhu thanks the financial support of Natural Science Foundation of China (21673063) and Natural Science Foundation of Heilongjiang Province (B2017005). M. Ni thanks the funding support from The Hong Kong Polytechnic University (G-YW2D) and a grant (Project Number: PolyU 152214/17E) from Research Grant Council, University Grants Committee, Hong Kong SAR.

REFERENCES

(1) Chow, J.; Kopp, R. J.; Portney, P. R. Energy Resources and Global Development. *Science* **2003**, *302* (5650), 1528–1531. DOI: 10.1126/science.1091939.

(2) Davies, D. M.; Verde, M. G.; Mnyshenko, O.; Chen, Y. R.; Rajeev, R.; Meng, Y. S.; Elliott, G. Combined Economic and Technological Evaluation of Battery Energy Storage for Grid Applications. *Nat. Energy* **2019**, *4* (1), 42–50. DOI: 10.1038/s41560-018-0290-1.

(3) Matter, J. M.; Stute, M.; Snæbjörnsdottir, S. Ó.; Oelkers, E. H.; Gislason, S. R.; Aradottir, E. S.; Sigfusson, B.; Gunnarsson, I.; Sigurdardottir, H.; Gunnlaugsson, E, Axelsson, G.; Alfredsson, H. A.; Wolff-Boenisch, D.; Mesfin, K.; Taya, D. F. de la R.; Hall, J.; Dideriksen, K.; Broecker, W. S. Rapid Carbon Mineralization for Permanent Disposal Ofanthropogenic Carbon Dioxide Emissions. *Science*

2016, *352* (6291), 1312–1314. DOI: 10.1126/science.aad8132.

(4) Peters, G. P.; Marland, G.; Le Quéré, C.; Boden, T.; Canadell, J. G.; Raupach, M. R. Rapid Growth in CO_2 Emissions after the 2008–2009 Global Financial Crisis. *Nat. Clim. Chang.* **2012**, *2* (1), 2–4. DOI: 10.1038/nclimate1332.

(5) Qie, L.; Lin, Y.; Connell, J. W.; Xu, J.; Dai, L. Highly Rechargeable Lithium-CO_2 Batteries with a Boron- and Nitrogen-Codoped Holey-Graphene Cathode. *Angew. Chemie Int. Ed.* **2017**, *56* (24), 6970–6974. DOI: 10.1002/anie.201701826.

(6) Wang, Z. L.; Xu, D.; Xu, J. J.; Zhang, X. B. Oxygen Electrocatalysts in Metal-Air Batteries: From Aqueous to Nonaqueous Electrolytes. *Chem. Soc. Rev.* **2014**, *43* (22), 7746–7786. DOI: 10.1039/c3cs60248f.

(7) Tan, P.; Jiang, H. R.; Zhu, X. B.; An, L.; Jung, C. Y.; Wu, M. C.; Shi, L.; Shyy, W.; Zhao, T. S. Advances and Challenges in Lithium-Air Batteries. *Appl. Energy* **2017**, *204*, 780–806. DOI: 10.1016/j.apenergy.2017.07.054.

(8) Cai, F.; Hu, Z.; Chou, S.-L. Progress and Future Perspectives on Li(Na)-CO_2 Batteries. *Adv. Sustain. Syst.* **2018**, *2* (8–9), 1800060. DOI: 10.1002/adsu.201800060.

(9) Xu, S.; Das, S. K.; Archer, L. A. The Li-CO2 Battery: A Novel Method for CO_2 Capture and Utilization. *RSC Adv.* **2013**, *3* (18), 6656–6660. DOI: 10.1039/c3ra40394g.

(10) Zhou, J.; Li, X.; Yang, C.; Li, Y.; Guo, K.; Cheng, J.; Yuan, D.; Song, C.; Lu, J.; Wang, B. A Quasi-Solid-State Flexible Fiber-Shaped Li–CO_2 Battery with Low

Overpotential and High Energy Efficiency. *Adv. Mater.* **2018**, *31* (3), 1804439. DOI: 10.1002/adma.201804439.

(11) Li, J.; Zhao, H.; Qi, H.; Sun, X.; Song, X.; Guo, Z.; Tamirat, A. G.; Liu, J.; Wang, L.; Feng, S. Drawing a Pencil-Trace Cathode for a High-Performance Polymer-Based Li–CO_2 Battery with Redox Mediator. *Adv. Funct. Mater.* **2019**, *29* (11), 1806863. DOI: 10.1002/adfm.201806863.

(12) Qi, H.; Sun, X.; Li, H.; Li, J.; Wang, Y.; Tamirat, A. G.; Liu, J.; Guo, Z.; Wang, L. A Highly Reversible Long-Life Li–CO_2 Battery with a RuP_2-Based Catalytic Cathode. *Small* **2018**, *15* (29), 1803246. DOI: 10.1002/smll.201803246.

(13) Xu, S.; Chen, C.; Kuang, Y.; Song, J.; Gan, W.; Liu, B.; Hitz, E. M.; Connell, J. W.; Lin, Y.; Hu, L. Flexible Lithium–CO_2 Battery with Ultrahigh Capacity and Stable Cycling. *Energy Environ. Sci.* **2018**, *11* (11), 3231–3237. DOI: 10.1039/c8ee01468j.

(14) Zhang, X.; Wang, C.; Li, H.; Wang, X. G.; Chen, Y. N.; Xie, Z.; Zhou, Z. High Performance Li-CO_2 Batteries with NiO-CNT Cathodes. *J. Mater. Chem. A* **2018**, *6* (6), 2792–2796. DOI: 10.1039/c7ta11015d.

(15) Liu, B.; Sun, Y.; Liu, L.; Chen, J.; Yang, B.; Xu, S.; Yan, X. Recent Advances in Understanding Li-CO_2 Electrochemistry. *Energy Environ. Sci.* **2019**, *12* (3), 887–922. DOI: 10.1039/c8ee03417f.

(16) Hu, A.; Shu, C.; Xu, C.; Liang, R.; Li, J.; Zheng, R.; Li, M.; Long, J. Design Strategies toward Catalytic Materials and Cathode Structures for Emerging Li-CO_2 Batteries. *J. Mater. Chem. A* **2019**, *7* (38), 21605–21633. DOI:

10.1039/c9ta06506g.

(17) Xiao, X.; Shang, W.; Yu, W.; Ma, Y.; Tan, P.; Chen, B.; Kong, W.; Xu, H.; Ni, M. Toward the Rational Design of Cathode and Electrolyte Materials for Aprotic Li-CO_2 Batteries: A Numerical Investigation. *Int. J. Energy Res.* **2020**, *44* (1), 496–507. DOI: 10.1002/er.4952.

(18) Xu, S. M.; Ren, Z. C.; Liu, X.; Liang, X.; Wang, K. X.; Chen, J. S. Carbonate Decomposition: Low-Overpotential Li-CO_2 Battery Based on Interlayer-Confined Monodisperse Catalyst. *Energy Storage Mater.* **2018**, *15*, 291–298. DOI: 10.1016/j.ensm.2018.05.015.

(19) Li, X.; Zhou, J.; Zhang, J.; Li, M.; Bi, X.; Liu, T.; He, T.; Cheng, J.; Zhang, F.; Li, Y.; Mu, X.; Lu, J.; Wang, B. Bamboo-Like Nitrogen-Doped Carbon Nanotube Forests as Durable Metal-Free Catalysts for Self-Powered Flexible Li–CO_2 Batteries. *Adv. Mater.* **2019**, *31*, 1903852. DOI: 10.1002/adma.201903852.

(20) Qiao, Y.; Liu, Y.; Chen, C.; Xie, H.; Yao, Y.; He, S.; Ping, W.; Liu, B.; Hu, L. 3D-Printed Graphene Oxide Framework with Thermal Shock Synthesized Nanoparticles for Li-CO_2 Batteries. *Adv. Funct. Mater.* **2018**, *28* (51), 1–7. DOI: 10.1002/adfm.201805899.

(21) Ahmadiparidari, A.; Warburton, R. E.; Majidi, L.; Asadi, M.; Chamaani, A.; Jokisaari, J. R.; Rastegar, S.; Hemmat, Z.; Sayahpour, B.; Assary, R. S.; Narayanan, B.; Abbasi, P.; Redfern P. C,; Ngo, A.; Vörös, M.; Greeley, J.; Klie, R.; Curtiss, L. A.; Salehi-Khojin, A. A Long-Cycle-Life Lithium–CO_2 Battery with Carbon Neutrality. *Adv. Mater.* **2019**, *31*, 1902518. DOI:

10.1002/adma.201902518.

(22) Zhao, H.; Li, D.; Li, H.; Tamirat, A. G.; Song, X.; Zhang, Z.; Wang, Y.; Guo, Z.; Wang, L.; Feng, S. Ru Nanosheet Catalyst Supported by Three-Dimensional Nickel Foam as a Binder-Free Cathode for Li-CO_2 Batteries. *Electrochim. Acta* **2019**, *299*, 592–599. DOI: 10.1016/j.electacta.2019.01.027.

(23) Mu, X.; Pan, H.; He, P.; Zhou, H. Li – CO_2 and Na – CO_2 Batteries : Toward Greener and Sustainable Electrical Energy Storage. *Adv. Mater.* **2019**, *1903790*, 1–22. DOI: 10.1002/adma.201903790.

(24) Zhao, Z.; Su, Y.; Peng, Z. Probing Lithium Carbonate Formation in Trace-O_2-Assisted Aprotic Li-CO_2 Batteries Using in Situ Surface-Enhanced Raman. *J. Phys. Chem. Lett.* **2019**, *10* (3), 322–328. DOI: 10.1021/acs.jpclett.8b03272.

(25) Qiao, Y.; Yi, J.; Wu, S.; Liu, Y.; Yang, S.; He, P.; Zhou, H. Li-CO_2 Electrochemistry: A New Strategy for CO_2 Fixation and Energy Storage. *Joule* **2017**, *1* (2), 359–370. DOI: 10.1016/j.joule.2017.07.001.

(26) Pipes, R.; Bhargav, A.; Manthiram, A. Phenyl Disulfide Additive for Solution-Mediated Carbon Dioxide Utilization in Li–CO_2 Batteries. *Adv. Energy Mater.* **2019**, *1900453*, 1–8. DOI: 10.1002/aenm.201900453.

(27) Wang, H.; Xie, K.; You, Y.; Hou, Q.; Zhang, K.; Li, N.; Yu, W.; Loh, K. P.; Shen, C.; Wei, B. Realizing Interfacial Electronic Interaction within ZnS Quantum Dots/N-rGO Heterostructures for Efficient Li–CO_2 Batteries. *Adv. Energy Mater.* **2019**, *9*, 1901806. DOI: 10.1002/aenm.201901806.

(28) Li, S.; Dong, Y.; Zhou, J.; Liu, Y.; Wang, J.; Gao, X.; Han, Y.; Qi, P.; Wang, B. Carbon Dioxide in the Cage: Manganese Metal-Organic Frameworks for High Performance CO_2 Electrodes in Li-CO_2 Batteries. *Energy Environ. Sci.* **2018**, *11* (5), 1318–1325. DOI: 10.1039/c8ee00415c.

(29) Zhang, X.; Zhang, Q.; Zhang, Z.; Chen, Y.; Xie, Z.; Wei, J.; Zhou, Z. Rechargeable Li-CO_2 Batteries with Carbon Nanotubes as Air Cathodes. *Chem. Commun.* **2015**, *51* (78), 14636–14639. DOI: 10.1039/c5cc05767a.

(30) Zhang, P. F.; Lu, Y. Q.; Wu, Y. J.; Yin, Z. W.; Li, J. T.; Zhou, Y.; Hong, Y. H.; Li, Y. Y.; Huang, L.; Sun, S. G. High-Performance Rechargeable Li-CO_2/O_2 Battery with Ru/N-Doped CNT Catalyst. *Chem. Eng. J.* **2019**, *363*, 224–233. DOI: 10.1016/j.cej.2019.01.048.

(31) Zhou, X.; Zhou, Z.; Wei, J.; Xie, Z.; Chen, Y.; Zhang, Q.; Zhang, Z.; Bao, J. The First Introduction of Graphene to Rechargeable Li–CO_2 Batteries. *Angew. Chemie Int. Ed.* **2015**, *54* (22), 6550–6553. DOI: 10.1002/anie.201501214.

(32) Ma, W.; Lu, S.; Lei, X.; Liu, X.; Ding, Y. Porous Mn2O3 Cathode for Highly Durable Li–CO_2 Batteries. *J. Mater. Chem. A* **2018**, *6* (42), 20829–20835. DOI: 10.1039/c8ta06143b.

(33) Yang, S.; Qiao, Y.; He, P.; Liu, Y.; Cheng, Z.; Zhu, J. J.; Zhou, H. A Reversible Lithium-CO_2 Battery with Ru Nanoparticles as a Cathode Catalyst. *Energy Environ. Sci.* **2017**, *10* (4), 972–978. DOI: 10.1039/c6ee03770d.

(34) Zhang, Z.; Zhang, Z.; Liu, P.; Xie, Y.; Cao, K.; Zhou, Z. Identification of Cathode Stability in Li-CO_2 Batteries with Cu Nanoparticles Highly Dispersed

on N-Doped Graphene. *J. Mater. Chem. A* **2018**, *6* (7), 3218–3223. DOI: 10.1039/c7ta10497a.

(35) Mao, Y.; Tang, C.; Tang, Z.; Xie, J.; Chen, Z.; Tu, J.; Cao, G.; Zhao, X. Long-Life Li–CO_2 Cells with Ultrafine IrO_2-Decorated Few-Layered δ-MnO_2 Enabling Amorphous Li_2CO_3 Growth. *Energy Storage Mater.* **2019**, *18*, 405–413. DOI: 10.1016/j.ensm.2018.08.011.

(36) Hou, Y.; Wang, J.; Liu, L.; Liu, Y.; Chou, S.; Shi, D.; Liu, H.; Wu, Y.; Zhang, W.; Chen, J. Mo_2C/CNT: An Efficient Catalyst for Rechargeable Li–CO_2 Batteries. *Adv. Funct. Mater.* **2017**, *27* (27), 1700564. DOI: 10.1002/adfm.201700564.

(37) Li, Y.; Zhou, J.; Zhang, T.; Wang, T.; Li, X.; Jia, Y.; Cheng, J.; Guan, Q.; Liu, E.; Peng, H.; Wang, B. Highly Surface-Wrinkled and N-Doped CNTs Anchored on Metal Wire: A Novel Fiber-Shaped Cathode toward High-Performance Flexible Li–CO_2 Batteries. *Adv. Funct. Mater.* **2019**, *1808117*, 1808117. DOI: 10.1002/adfm.201808117.

(38) Xing, Y.; Yang, Y.; Li, D.; Luo, M.; Chen, N.; Ye, Y.; Qian, J.; Li, L.; Yang, D.; Wu, F.; Chen, R.; Guo, S. Crumpled Ir Nanosheets Fully Covered on Porous Carbon Nanofibers for Long-Life Rechargeable Lithium–CO_2 Batteries. *Adv. Mater.* **2018**, *30* (51), 1803124. DOI: 10.1002/adma.201803124.

(39) Ottakam Thotiyl, M. M.; Freunberger, S. A.; Peng, Z.; Bruce, P. G. The Carbon Electrode in Nonaqueous Li-O_2 Cells. *J. Am. Chem. Soc.* **2013**, *135* (1), 494–500. DOI: 10.1021/ja310258x.

(40) Qiao, Y.; Ye, S. Spectroscopic Investigation for Oxygen Reduction and Evolution Reactions on Carbon Electrodes in Li-O_2 Battery. *J. Phys. Chem. C* **2016**, *120* (15), 8033–8047. DOI: 10.1021/acs.jpcc.6b01784.

(41) Tan, P.; Wei, Z. H.; Shyy, W.; Zhao, T. S.; Zhu, X. B. A Nano-Structured RuO_2/NiO Cathode Enables the Operation of Non-Aqueous Lithium-Air Batteries in Ambient Air. *Energy Environ. Sci.* **2016**, *9* (5), 1783–1793. DOI: 10.1039/c6ee00550k.

(42) Mahne, N.; Fontaine, O.; Thotiyl, M. O.; Wilkening, M.; Freunberger, S. A. Mechanism and Performance of Lithium-Oxygen Batteries – a Perspective. *Chem. Sci.* **2017**, *8* (10), 6716–6729. DOI: 10.1039/c7sc02519j.

(43) Zhang, P.; Zhao, Y.; Zhang, X. Functional and Stability Orientation Synthesis of Materials and Structures in Aprotic Li-O_2 Batteries. *Chem. Soc. Rev.* **2018**, *47* (8), 2921–3004. DOI: 10.1039/c8cs00009c.

(44) Benitez, L.; Seminario, J. M. Ion Diffusivity through the Solid Electrolyte Interphase in Lithium-Ion Batteries. *J. Electrochem. Soc.* **2017**, *164* (11), E3159–E3170. DOI: 10.1149/2.0181711jes.

(45) Ebrahiminia, M.; Hooper, J. B.; Bedrov, D. Structural, Mechanical, and Dynamical Properties of Amorphous Li_2CO_3 from Molecular Dynamics Simulations. *Crystals* **2018**, *8* (12), 473. DOI: 10.3390/cryst8120473.

(46) Tian, F.; Radin, M. D.; Siegel, D. J. Enhanced Charge Transport in Amorphous Li_2O_2. *Chem. Mater.* **2014**, *26* (9), 2952–2959. DOI: 10.1021/cm5007372.

(47) Hu, X.; Li, Z.; Chen, J. Flexible Li-CO_2 Batteries with Liquid-Free Electrolyte.

Angew. Chemie Int. Ed. **2017**, *56* (21), 5785–5789. DOI: 10.1002/anie.201701928.

(48) Zhang, S. S.; Xu, K.; Jow, T. R. Effect of Li_2CO_3-Coating on the Performance of Natural Graphite in Li-Ion Battery. *Electrochem. commun.* **2003**, *5* (12), 979–982. DOI: 10.1016/j.elecom.2003.09.014.

(49) Qiu, F.; Ren, S.; Mu, X.; Liu, Y.; Zhang, X.; He, P.; Zhou, H. Towards a Stable Li-CO_2 Battery: The Effects of CO_2 to the Li Metal Anode. *Energy Storage Mater.* **2019**. DOI: 10.1016/j.ensm.2019.11.017.

(50) Lu, S.; Shang, Y.; Ma, S.; Lu, Y.; Liu, Q. C.; Li, Z. J. Porous NiO Nanofibers as an Efficient Electrocatalyst towards Long Cycling Life Rechargeable Li–CO_2 Batteries. *Electrochim. Acta* **2019**, *319*, 958–965. DOI: 10.1016/j.electacta.2019.07.062.

(51) Liu, W.; Shen, Y.; Yu, Y.; Lu, X.; Zhang, W.; Huang, Z.; Meng, J.; Huang, Y.; Guo, Z. Intrinsically Optimizing Charge Transfer via Tuning Charge/Discharge Mode for Lithium–Oxygen Batteries. *Small* **2019**, *15* (19), 1–8. DOI: 10.1002/smll.201900154.

Table of content graphic

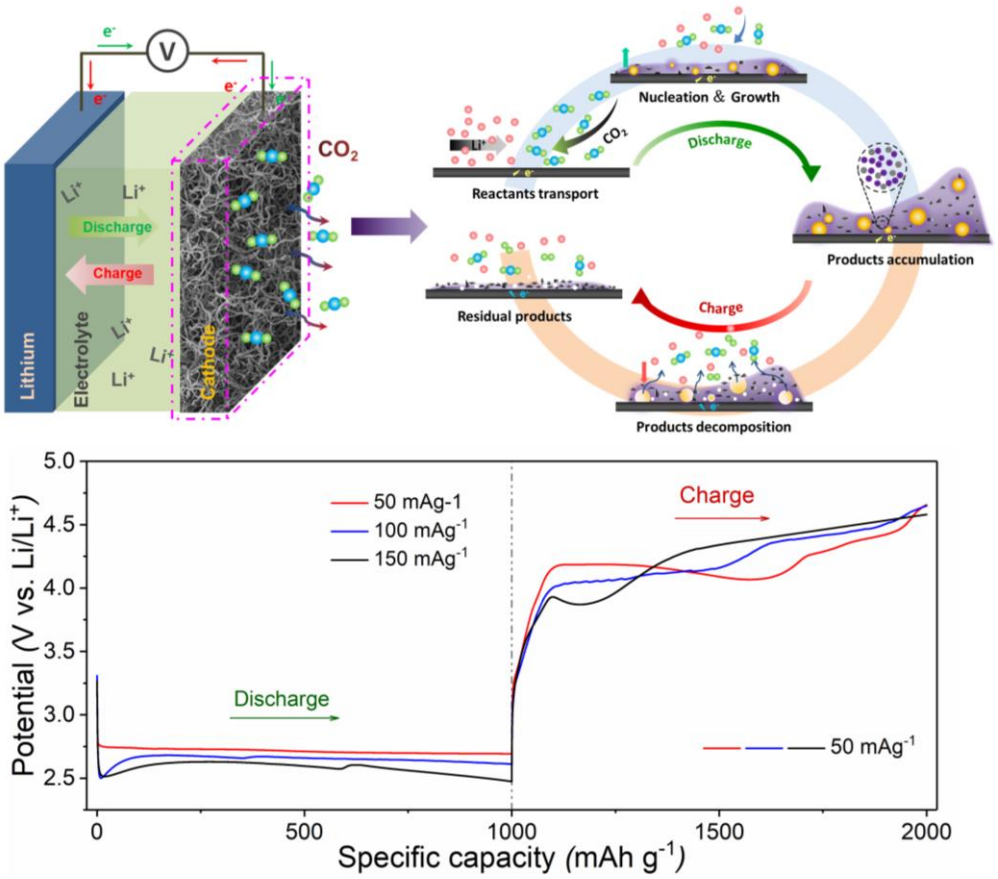

For Table of Contents Use Only

The discharge and charge behaviors of Li-CO_2 batteries with carbon nanotube electrodes are investigated in this work.